Article

Controlling Lateral Size and Thickness of Layered Double Hydroxide (LDH) Used as Conversion Layer for Corrosion Protection of AZ31 Mg Alloy

Roya Malekkhouyan [1], Yoann Paint [2], Loïc Prince [1], Maurice Gonon [1] and Marie-Georges Olivier [1,2,*]

[1] Materials Science Department, UMONS-University of Mons, Place du Parc 20, B-7000 Mons, Belgium
[2] Materia Nova asbl, Avenue Nicolas Copernic 3, B-7000 Mons, Belgium
* Correspondence: marjorie.olivier@umons.ac.be

Abstract: In the present study, Mg-Al layered double hydroxide (Mg-Al/LDH) was synthesized on the surface of AZ31 Mg alloy substrate via in-situ hydrothermal treatment. Synthesis parameters were changed to determine their effect on the lateral size of LDH. For this purpose, etching in nitric acid and anodizing in sodium hydroxide solution were performed as surface pretreatments. Moreover, the influence of LDH solution pH (10 and 11) on the lateral size of LDH coating was investigated. Morphology, chemical composition, and crystalline structure were characterized by scanning electron microscopy (SEM), energy-dispersive X-ray spectroscopy (EDS), Fourier transform infrared (FTIR) spectroscopy, and X-ray diffraction (XRD). The corrosion resistance of the coatings was investigated by H_2 measurements, salt spray, and electrochemical impedance spectroscopy (EIS). Moreover, the epoxy coating was applied on the best anti-corrosive LDH sample for assessing the compatibility and effectiveness of LDH on the corrosion properties of the substrate with the epoxy layer. At pH = 11, the lateral size of LDH was smaller than samples at pH = 10. In addition, small-sized LDH, as well as LDH/epoxy coating, revealed enhanced corrosion protection.

Keywords: Magnesium; corrosion; conversion coating; layered double hydroxide; epoxy

1. Introduction

The global market of magnesium alloys is expected to grow at the rate of 9.9% (compound annual growth rate (CAGR)) from 2020 to 2027 [1]. They are used in different industries as well as academic studies including biomedical devices, automotive, and aerospace sectors thanks to their high strength/weight ratio, machinability, good electrical and thermal conductivities. However, their usage has been limited due to their poor corrosion resistance [2,3]. Magnesium tends to corrode in aqueous electrolytes due to the low standard potential (-2.37 V_{SHE}). However, the actual corrosion potential (-1.7 V_{SHE}) is different from the standard potential as the result of the formation of an oxide/hydroxide layer on the surface. The formation of this oxide layer can be explained using the Pourbaix diagram. According to this diagram, for pH values more than 9, $Mg(OH)_2$ can be precipitated on the surface [4]. The corrosion of Mg alloys depends on the alloy composition as well as the environment. Second phases or impurities in Mg alloys can create micro-cells in presence of electrolytes and increase corrosion. Moreover, the passive layer on Mg alloy is not as protective as passive layers formed on other metals like aluminum and stainless steel and has only low corrosion resistance [4].

For these reasons, different strategies have been used for increasing the corrosion resistance of Mg alloys such as increasing aluminum content [5], decreasing impurities content [4], using rapid solidification for leading to a homogenous structure [6], and application of organic coating. Organic coatings are the most cost effective method in the industry for the protection of Mg alloys [7]. As a barrier layer, organic coatings have the ability to prevent Mg alloys from corrosion. However, the adhesion of the organic coating to

the substrate should be increased by appropriate surface treatment to enhance the corrosion resistance of the substrate [8,9]. Surface treatments before applying organic coatings not only affect the adhesion but also the roughness, and film formation process [10]. These treatments include electroless plating [7], conversion layers [11,12], anodic oxidation [2,8], and so on. Anodization is among the well-known and facile techniques which can enhance wear and corrosion resistance [13]. However, due to the porous and brittle structure of anodic coatings, further modification is required. Layered double hydroxide (LDH) has been found as an effective method for improving the corrosion resistance of Mg alloys which can be used for sealing the anodic layer as well [14–16].

LDH is also known as anionic clays and hydrotalcite (hydro for water content and talcite for resembling talc) which can be formed with different combinations of metals and anions [17]. The chemical formula of LDH is presented by $[M(II)_{1-x} M(III)_x (OH)_2]^{x+}$ $(A^{n-})_{x/n} \cdot yH_2O$ in which M(II) and M(III) are divalent and trivalent metal cations that form octahedral structure with A^{n-} as an interlayer anion, and the stoichiometric coefficient of x [17,18]. The appropriate ratio of metals is between 2:1 to 4:1 leading to the x range of 0.2 to 0.33. LDHs can be produced by facile methods and give corrosion resistance to the substrate by having high loading capacity as well as anion exchangeability which makes them suitable for practical usages [18]. When LDH coatings are in contact with corrosive media, interlayered anions can be released, and simultaneously corrosive species are adsorbed [19]. Despite the abovementioned properties of LDH coatings, their production on magnesium alloys has some limitations. They should be produced under high pressure and temperature. Moreover, pre-formed LDH which is not produced on the surface of substrates directly has low adhesion to the substrate [20].

The corrosion performance of the LDH layer is strongly dependent on the substrate, surface treatment before production of LDH, concentration, and type of cations involved in the synthesis process, pH of LDH solution, hydrothermal treatment time, and temperature which can modify the morphology, crystallinity, size, and thickness of LDH [14,15,21,22]. Asl et al. [23] worked on the production of Mg-Ce/LDH. They showed that using Ce ions in the structure of LDH can enhance corrosion resistance by forming deposited cerium hydroxide at defects. Wu et al. [21] investigated the effect of different cations on the anti-corrosion property of LDH produced by in-situ hydrothermal treatment at 125 °C. They observed that Mg-Al LDH had the highest protective properties in comparison to Mg-Fe and Mg-Cr LDH. In another study [14], they showed that the LDH layer performance was increased when produced at pH between 10 and 11. XRD diagrams at pH less than 10, showed the high intensity of the Mg peak while there was no peak for $Mg(OH)_2$, representing that Mg ions are not present in sufficient quantity for participating in the LDH structure. For the LDH layer prepared at pH more than 11 (around 12), the intensity of XRD peaks related to LDH and impedance modulus of the LDH layer at low frequency was decreased in comparison to LDH prepared at pH = 10.72 and 11.72 [14]. It was shown that increasing hydrothermal treatment temperature can enhance the structure and make the LDH layer denser [15].

In previous studies, the approximate Mg-Al/LDH flake size was around 1 to 2 μm prepared on anodized and grinded substrates [14,15,24]. However, to the best of our knowledge, the effect of LDH lateral size on the corrosion resistance of the substrate has not been reported yet. Rojas [25] used magnesium-aluminum LDH (Mg-Al/LDH) with intercalated carbonate for the removal of Cu cations and showed that decreasing size can increase buffering capacity due to the higher surface area. Therefore, there should be studies related to optimizing the size of LDH to increase their efficiency.

Only a few studies were related to the investigation of a complete protective system on magnesium alloys combining a LDH conversion layer and an epoxy coating [26]. In this study, Mg-Al/LDH layer is produced on AZ31 magnesium alloy submitted to different surface treatments: etching and anodizing. The hydrothermal treatment was performed at two pH in the alkaline region of pH (10 and 11). Physical and chemical characteristics of LDH were observed by SEM, EDS, XRD, and FTIR. Electrochemical impedance spectroscopy,

H_2 production, and salt spray tests were carried out for assessing corrosion behavior. The effect of LDH lateral size as well as the surface pretreatment on the corrosion behavior of the substrate was investigated by measuring the volume collected hydrogen and EIS tests to achieve the most efficient LDH. After characterizing LDH, the best corrosion-resistant sample was used for assessing the effect of the LDH layer as a conversion layer on the corrosion performance of applied epoxy on the substrates by salt spray test. It was observed that the small-sized LDH produced at pH = 11 can have good compatibility with the epoxy layer and improved corrosion resistance of the substrate.

2. Materials and Methods

2.1. Materials and Surface Treatments

AZ31 magnesium alloy was used as substrate with composition of 2.5–3.5% Al, 0.7–1.3% Zn, 0.2% Mn, 0.05% Si, 0.05% Cu, 0.04% Ca, 0.005% Fe, 0.1% Ni (wt %) and balance Mg (supplied from KG Fridman AB (SWEDEN)). The microstructure of the substrate was reported in our previous study [27]. NH_4NO_3, $Al(NO_3)_3.9H_2O$, NaOH, and NaCl were purchased from RPL, EMPLURA, VWR Chemicals, and LAMERS AND PLEUGER, respectively. The commercial resin Epikote 828 (Brenntag) with an equivalent weight of 185–192 g/eq was used as epoxy resin. Diluent Epotec RD 106 para-tertialy butyl phenyl glycidyl ether (ThaiEpoxy group) with an equivalent weight of 220–250 g/eq was added to reduce the viscosity of the resin. The amine curing agent was Ancamine 2753, 3-aminoethyl-3,5,5 trimethylcyclohexylamine (Air product) with an equivalent weight per active H of 153 g/eq.

AZ31 Mg alloy substrates with dimensions of $1 \times 37 \times 50$ mm were first etched for 30 s in 2 M HNO_3 solution, and then again etched for 60 s in 0.25 M HNO_3 before rinsing in deionized water [27]. Etching can remove the oxide layer and make micron to nano-sized roughness on the surface for increasing wettability [28]. In the end, the samples were dried under a stream of air.

After pretreatment of substrates in acid, several samples were anodized by DC-regulated power in a continuously stirred 2 M NaOH solution for 15 minutes under a low stable voltage of 4 V. The anodized substrates (with a thickness of 10 ± 2 μm) were rinsed with water and dried with air.

The LDH was synthesized on the pretreated surface of substrates using the in-situ hydrothermal treatment method in a Teflon-lined autoclave at 125 °C for 24 h at different pH solutions. Table 1 shows the conditions and codes used for samples. Specimens were immersed in the solution containing 0.1 M $Al(NO_3)_3$ and 0.6 M NH_4NO_3. The pH of the solution was adjusted by the slow addition of 2 M NaOH while stirring before immersing samples. Figure 1 shows the procedure for producing LDH.

Table 1. Codes used for LDH samples.

Surface Treatment	pH	Code
Etched Substrate	10	E1024
	11	E1124
Anodized Substrate	10	A1024
	11	A1124

Epoxy resin, diluent, and hardener were used with the ratio of 10:5:3 for applying epoxy on the substrates. First, epoxy resin was mixed with diluent overnight and then hardener was added to the solution and mixed for 1 min. The epoxy coating was applied on the substrates using dip coater (KSV NIMA) with the speed of 600 mm/min and the samples were immersed in the solution for 30 s. Samples were kept at room temperature (23 ± 0.5 °C) for 1 day and were then post-cured at 120 °C for 1 hour. The thickness of the epoxy coating after curing was 12 ± 2 μm (measured by SEM). The samples were coded according to Table 2.
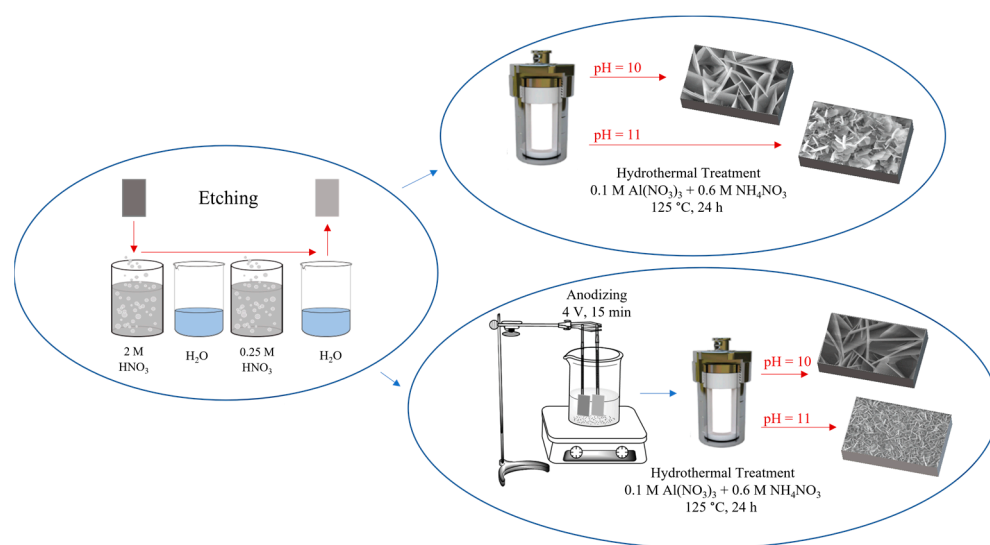
Figure 1. Schematic image of LDH production.

Table 2. Codes used for samples with epoxy coating.

Surface Treatment	Code of Samples with Epoxy Coating
Etched	E/Epoxy
Anodized	A/Epoxy
LDH (coded according to Table 1)	A1124/Epoxy

2.2. Characterization Techniques

The surface and cross-section morphologies, as well as the elemental composition of LDHs, were investigated by scanning electron microscope (SEM, Hitachi SU8020) equipped with an energy dispersive X-ray spectrometer analyzer (EDS, Thermo Scientific Noran System 7). For cross-section images, samples were embedded in resin (EpoFix resin and EpoFix hardener) and were grounded with 800, 1200, 2000, and 4000 SiC papers using Struer TegraForce-5. The thickness of samples and the lateral size of LDH was measured using ImageJ software from SEM images. Fourier-transform infrared spectroscopy (FTIR, Shimadzu IRTracer-100) in reflectance mode, in the wavenumber range from 500 to 4000 cm^{-1} at room temperature (23 ± 0.5 °C) was used to determine chemical groups. The LDH crystalline structures were investigated with X-ray diffraction (XRD, Panalytical Empyrean Theta–Theta) with CuKα radiation ($\lambda = 0.154056$ nm) and Ni filter with a step of $0.02°$ and a scanning rate of $1.2°$/min in the 2θ range from $8°$ to $70°$.

Hydrogen evolution experiments were carried out on samples with dimensions $1 \times 37 \times 37$ mm in 100 mL of 0.1 M NaCl solution using eudiometers supplied by Neubert-Glas (NEUB2591). All tests were performed for 7 days at room temperature (23 ± 0.5 °C) without interruption and the volume of released hydrogen was recorded visually. The volume of resided or dissolved hydrogen in 0.1 M NaCl was ignored as the solubility of H$_2$ in water is too low. The volume of released hydrogen was divided by surface area in contact with the NaCl solution. The collected hydrogen rate can be converted to the mass loss rate due to the production of one H$_2$ molecule by dissolving one atom of Mg using the ideal gas law [29,30].

The electrochemical impedance spectroscopy was performed in 0.1 M NaCl solution using a ModulLab controlled by XM-Studio®software. A classical three-electrode system, which consisted of a platinum counter electrode, an Ag/AgCl (sat. KCl) reference electrode, and AZ31 Mg alloy samples, as working electrodes with an exposed area of 1 cm^2 were used. EIS measurements were performed in a frequency range from 100 kHz to 100 mHz with 61 points using a 10 mV peak-to-peak sinusoidal voltage. Each experiment was performed at least three times.

For investigating the qualitative adhesion of the LDH to the substrate a tape with a size of 25 mm × 66 m supplied by Rubans de Normandie (8705B) was adhered to the samples on a stable holder. After 30 s, the tape was manually removed before SEM observation of the surface. Salt spray test was also performed (Q-LAB Model SSP) according to the ASTM B117 on intact and x-cut scratched samples with a width of 100 μm and angle of 30°.

3. Results

3.1. Physical and Chemical Characteristics of LDHs

To investigate the effect of experimental parameters on the morphology of coatings, SEM micrographs were determined. Figure 2 shows SEM images of the anodized and LDH structure on substrate samples. Figure 2 exhibits the blade-like surface of LDHs and their uniform and dense structure growth on Mg alloy substrates. In Figure 2a it can be seen that the cracks and micropores of the anodic layer are sealed with LDH structure in Figure 2d,e. According to Figure 2e, the LDH lateral size of sample A1124 is about eight times smaller than other samples (the lateral size for A1124 and A1024 is 0.16 ± 0.03 μm and 1.3 ± 0.4 μm, respectively). Moreover, at pH = 11 the structure is more compact and tangled. LDH layers consist of a compact inner layer and a porous outer layer [31,32]. The cross-section images of samples at different magnifications (Figure 2g–n) for both LDHs on etched and anodized substrates show the lower outer layer and higher inner layer thickness of LDH produced at pH = 11. 10 measurements were carried out for each sample and the average thickness is shown in Table 3. As can be seen in the micrographs, the lower outer layer thickness is attributed to the smaller lateral size of LDH sheets. Open spaces in larger lateral size LDH at pH = 10 can be observed vividly (these spaces are filled with epoxy in the images) while these spaces are too small and more compact for LDH at pH = 11. So even the thickness of the outer layer at pH = 11 is less than pH = 10, the structure is more compact. Surface treatment did not change the morphology of LDH considerably. For the formation of LDH, the Mg bivalent cation is supplied by the substrate and the Al trivalent cation is furnished by the electrolyte.

Table 3. Approximate LDH lateral size and thickness of different layers.

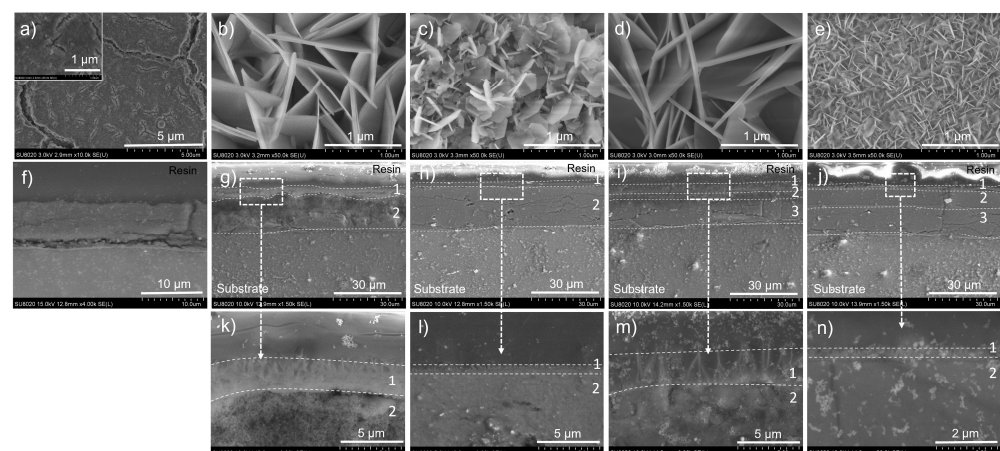| Sample Code	E1024	E1124	A1024	A1124
Approximate LDH lateral size (μm)	1.5 ± 0.2	0.18 ± 0.06	1.3 ± 0.4	0.16 ± 0.03
Thickness of porous outer layer (μm)	2.8 ± 0.2	0.7 ± 0.1	3.2 ± 0.2	0.4 ± 0.03
Thickness of compact inner layer (μm)	15.3 ± 0.5	18.8 ± 0.2	2.7 ± 0.2	7.7 ± 0.2
Thickness of anodic layer (μm)	-	-	11 ± 0.5	11.1 ± 0.4

Figure 2. SEM images of surface: (**a**) anodized, (**b**) E1024, (**c**) E1124, (**d**) A1024, (**e**) A1124, cross-section: (**f**) anodized, (**g**) E1024, (**h**) E1124, (**i**) A1024, (**j**) A1124, and cross-section with higher magnification: (**k**) E1024, (**l**) E1124, (**m**) A1024, (**n**) A1124. ((1): porous outer layer, (2): compact inner layer, (3): anodic layer).

EDS mapping from the cross-section of samples as well as EDS graphs in Figure 3 show the elemental mapping of Mg, Al, and O. Al elemental distribution shows high concentration at the top layer which proves the formation of LDH. EDS graphs for etched samples are from the compact inner layer while for anodized samples are from the anodic plus compact inner layer (EDS graphs of the porous outer layer couldn't give us useful information as there is epoxy between the LDH sheets) which show the low concentration of Al element at these layers.
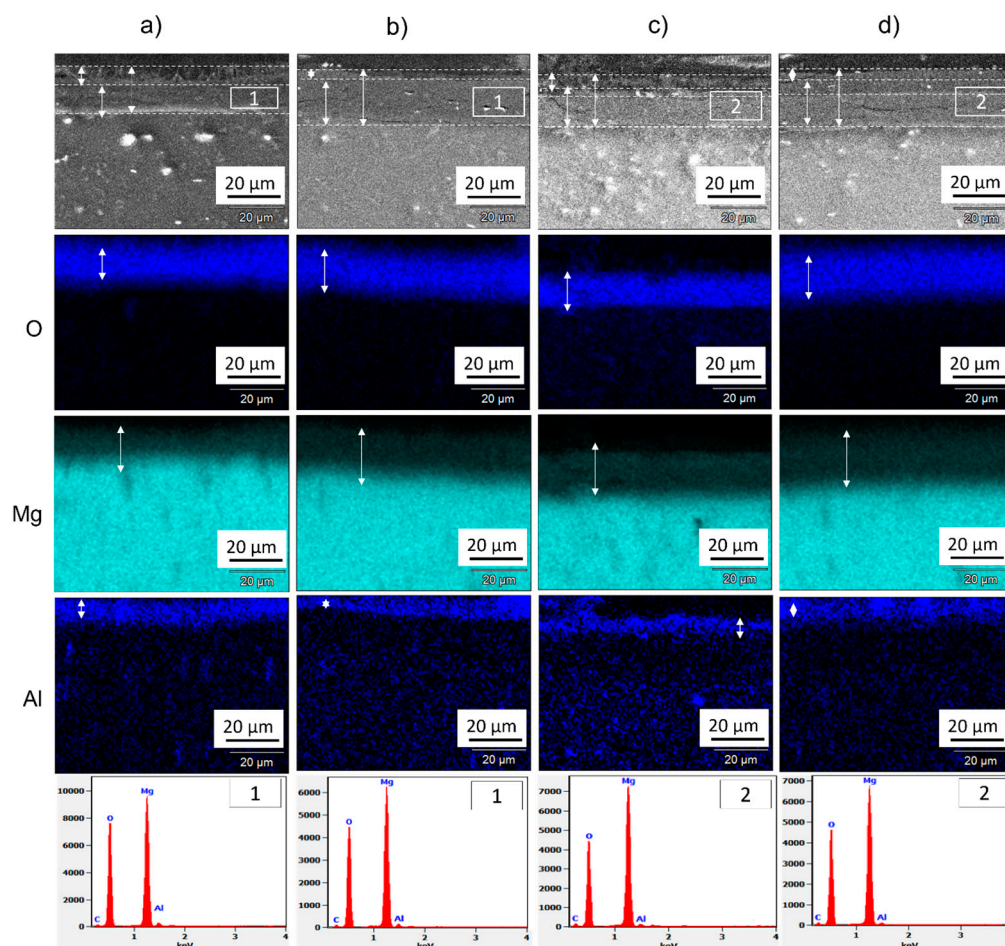

Figure 3. EDS mapping and EDS graphs of the cross-section of (**a**) E1024, (**b**) E1124, (**c**) A1024, and (**d**) A1124 (box 1 from the inner layer and box 2 from the inner and anodized layers).

Figure 4 shows the FTIR spectra of samples produced with different parameters. The broad band at 3000–3500 cm^{-1} can be attributed to the OH stretching vibration of absorbed water. Bands corresponding to the H-O-H stretching vibration are at approximately 3695 cm^{-1}. Another absorption band recorded at about 1641 cm^{-1} is attributed to the bending vibration of water molecules. The band at around 1370 cm^{-1} and 1366 cm^{-1} for the samples with LDH can be associated to CO_3^{2-} or NO_3^-, respectively, according to Wu et al. [21]. However, FTIR method is not reliable for demarcating NO_3^- and CO_3^{2-} when they are intercalated in LDH structure [33]. Therefore, determination of the intercalated anion can be done more accurately using XRD results and the crystal size of LDH. The existence of characteristic peaks for NO_3^- or CO_3^{2-} only in samples with LDH proves their formation [21]. The spectral peaks in the range 444~770 cm^{-1} correspond to the lattice vibration absorption peaks of LDH metal-oxygen bonds (M-O, M-O-M, and O-M-O) [14,21].
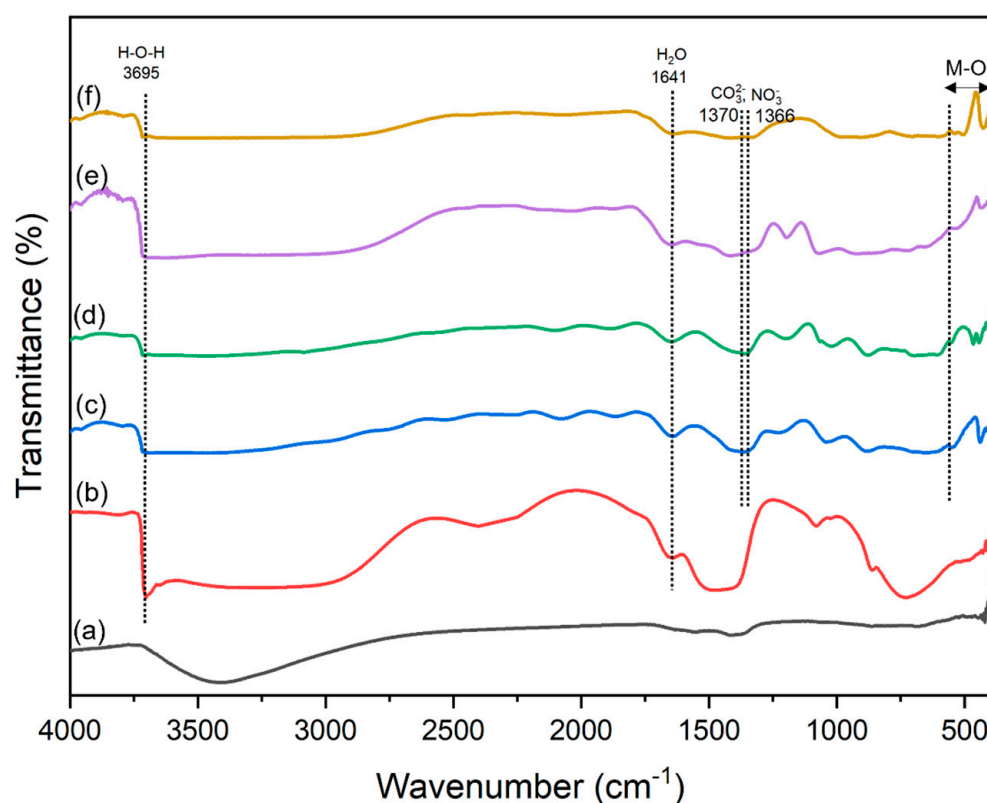
Figure 4. FT–IR spectrum of (**a**) etched, (**b**) anodized, (**c**) E1024, (**d**) E1124, (**e**) A1024, and (**f**) A1124.

XRD patterns of samples are shown in Figure 5. The characteristic peaks of Mg, $Mg(OH)_2$, and LDH are marked in the figure according to JCPDS No. 00-035-0821, 00-007-0239 and 00-014-0191, respectively. $Mg(OH)_2$ peak at 38.02° shows the dissolution of Mg for the production of LDH [14]. The obtained peaks for samples were compared with patterns related to $Mg_6Al_2(CO_3)(OH)_{16} \cdot 4H_2O$. The characteristic diffraction peaks of hydrotalcite at (003) were observed in XRD patterns at around 11°, however, peaks at (006) could not be seen vividly. According to the literature, the intensity of (006) LDH peak is less than (003) [14,21]. In this case, the (006) peak may be too small to be seen. Samples A1024 and E1024 have more intense peaks in comparison to A1124, which can be due to the thicker porous outer layer LDH for samples at pH = 10. The size of intercalated anions and the stacking direction determine the interlayer spacing. In the reaction for the formation of LDH coating, CO_3^{2-} anions can be supplied by the dissolution of CO_2 gas [14]. Table 4 shows the d-spacing related to the samples. According to Table 4, c parameter (3d(003) = c) is 23.007 A° for A1124 which can be related to the CO_3^{2-} or OH^-, while this amount is 24.35 A° and 24.087 A° for A1024 and E1024, respectively, relating to the intercalated NO_3^- [34]. It can be inferred that preparing the sample at pH = 11 not only affects (decreases) the lateral size but also the crystal unit cell. In the study of Wang et al. [35] it was shown that decreasing Mg:Al ratio for synthesizing LDH could increase the basal spacing of LDH. The concentration of Mg can affect the layer charge density and change the configuration of the intercalated anion [35]. Therefore, the lower d-spacing for A1124 can be the result of higher Mg cations concentration at the same Al concentration in LDH solution for all of the samples (explained in more detail in Discussion section) and changes in the charge density of the layers.
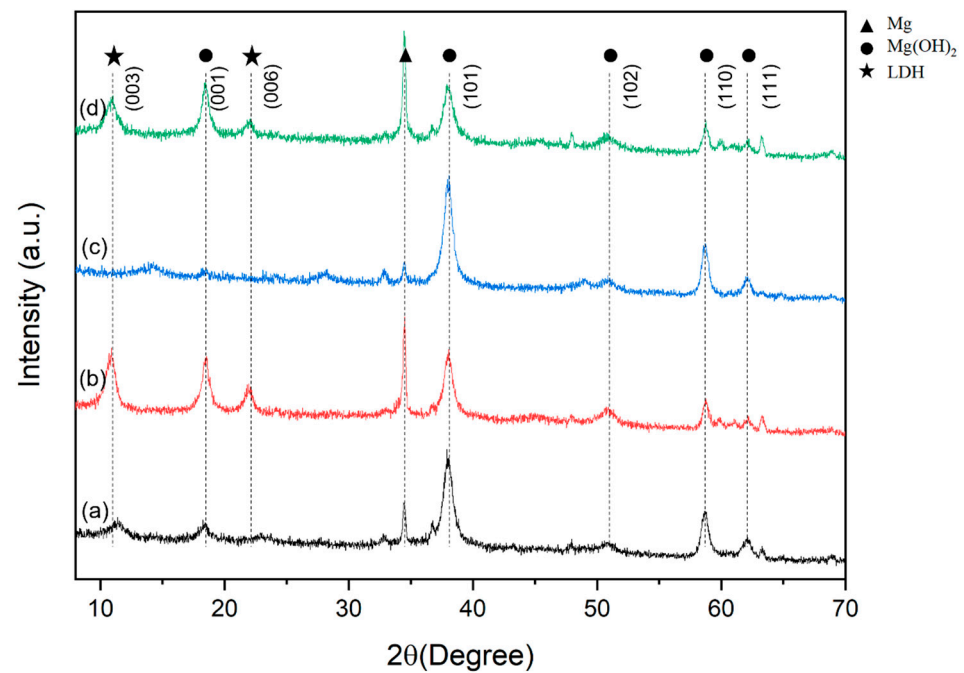
Figure 5. XRD diagrams of (**a**) A1124, (**b**) A1024, (**c**) E1124, and (**d**) E1024, before immersion.

Table 4. The d-spacing corresponding to the (003) plane for samples.

Sample Code	Before Immersion				After Immersion			
	E1024	E1124	A1024	A1124	E1024	E1124	A1024	A1124
d(003) (Å)	8.029	–	8.117	7.669	7.934	–	7.661	7.715

The qualitative adhesion of LDH to the substrates was investigated using tape. For this purpose, SEM images were taken before and after applying the tape. According to Figure 6, after peeling off the tape, for samples prepared at pH = 10, the LDH was removed from the substrate showing low adhesion to the substrate. However, for A1124 and E1124 samples peeling off the tape was hard and there was still LDH on the surface after removing the tape (only a small part of LDH was removed for sample E1124 which is shown in Figure 6f). Moreover, for A1124 residuals of tape were stuck on the surface showing the applicability of this sample for further use of organic coating on it.
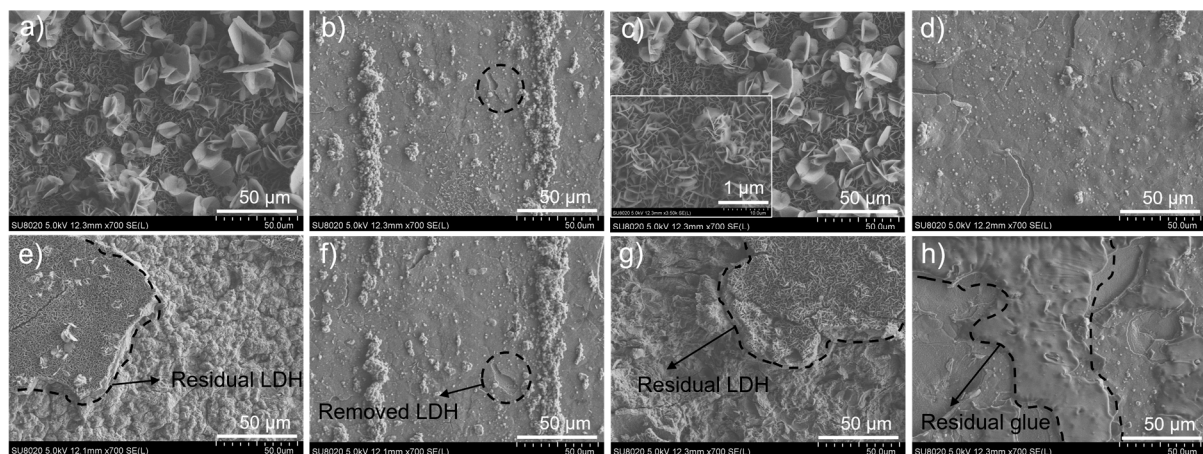

Figure 6. SEM images of (**a**) E1024, (**b**) E1124, (**c**) A1024, (**d**) A1124, before applying the tape and (**e**) E1024, (**f**) E1124, (**g**) A1024, (**h**) A1124 after peeling off. 3.2. Physical and Chemical Characteristics of LDH After Immersion in 0.1 M NaCl for 7 Days.

SEM micrographs of the samples' surface after immersion in 0.1 M NaCl solution for 7 days are presented in Figure 7. According to these micrographs, after 7 days no corrosion pits are seen. The SEM images exhibit that the coating still has a very typical nanosheet structure of LDH phases without evident damage. Compared to the SEM images of LDH films before immersion, the change is the LDH structure transformed from sharp to rounded edges (shown with circles in Figure 7), especially for samples E1024 and A1024, which is due to the dissolution of LDH edges. Moreover, the lateral size of LDH prepared at pH = 11 was increased after immersion as the result of the substrate dissolution and LDH recrystallization [36].
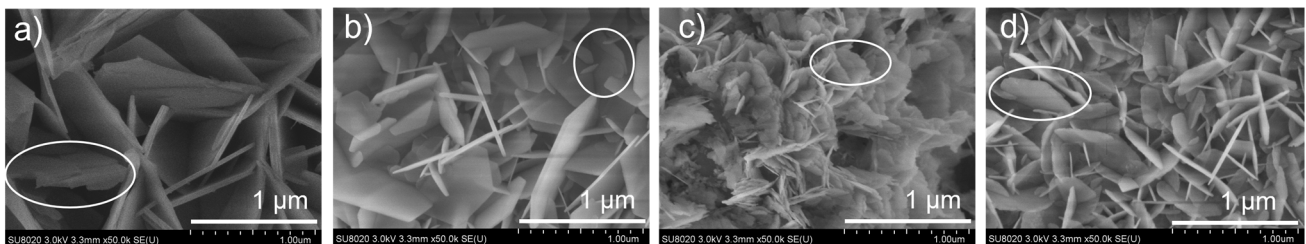

Figure 7. SEM images of surface (**a**) E1024, (**b**) E1124, (**c**) A1024, (**d**) A1124, after immersion in 0.1 M NaCl solution for 7 days.

EDS mappings of the surface of the sample after immersion in 0.1 M NaCl solution for 7 days are shown in Figure 8 which shows the adsorption and maintenance of Cl$^-$ ions by LDH [22,37].
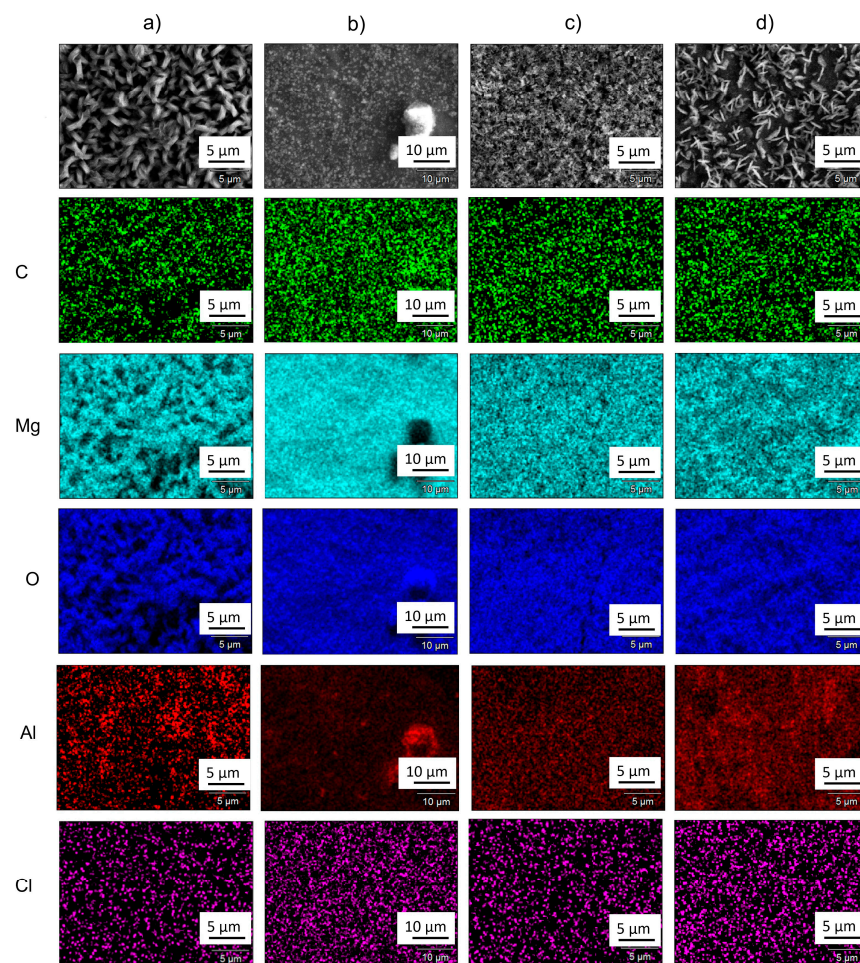

Figure 8. EDS mapping of surface of (**a**) E1024, (**b**) E1124, (**c**) A1024, and (**d**) A1124 after immersion in 0.1 M NaCl solution for 7 days.

Figure 9 shows XRD for samples after immersing in 0.1 M NaCl solution for 7 days. The existence of LDH characteristic peaks at (003) and (006), after immersion, shows that even after immersion for 7 days we still have LDH structure on the substrates.
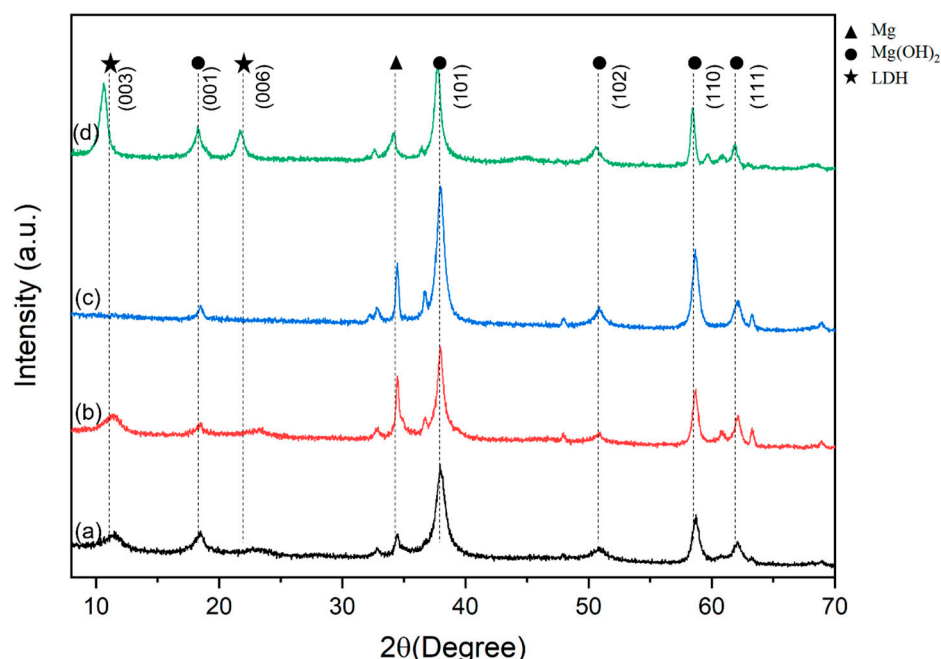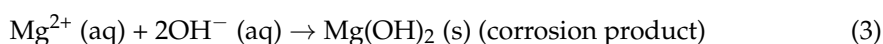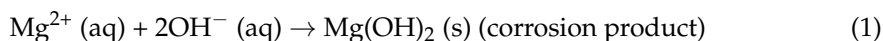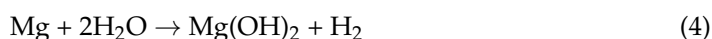

Figure 9. XRD diagrams of (**a**) A1124, (**b**) A1024, (**c**) E1124, and (**d**) E1024, after 7 days immersion in 0.1 M NaCl solution.

The d-spacing for A1124 is increased after immersion. By considering intercalated CO_3^{2-} or OH^- anions as the result of data obtained before immersion, the increase in d-spacing can be related to the dissolution and recrystallization of LDH with intercalation of Cl^- anion. This result is in agreement with previous studies [22]. However, for A1024 and E1024 the d-spacing was decreased as the intercalated anion is changed from NO_3^- to Cl^-. XRD along with EDS results after immersion can show the intercalation of Cl anions in the LDH structure [22,38]. For sample E1124 before and after immersion characteristic peaks of LDH at (003) and (006) could not be observed due to the thin LDH outer layer. Moreover, the increased intensity of $Mg(OH)_2$ peak at around $38°$ in all the samples (in comparison to the Mg peak at around $34.5°$), implies the occurrence of substrate corrosion according to the reactions below [5].

$$Mg^{2+} \text{ (aq)} + 2OH^- \text{ (aq)} \rightarrow Mg(OH)_2 \text{ (s) (corrosion product)} \qquad (1)$$

$$2H_2O + 2\,e^- \rightarrow H_2 + 2\,OH^- \qquad (2)$$

$$Mg^{2+} \text{ (aq)} + 2OH^- \text{ (aq)} \rightarrow Mg(OH)_2 \text{ (s) (corrosion product)} \qquad (3)$$

Which leads to the overall reaction of:

$$Mg + 2H_2O \rightarrow Mg(OH)_2 + H_2 \qquad (4)$$

3.2. H_2 Evolution Experiment

In Figure 10, The collected hydrogen from eudiometer for etched and anodized as well as LDH samples after immersion in 0.1 M NaCl solution for 7 days, is expressed as the unit of mL per cm^2.
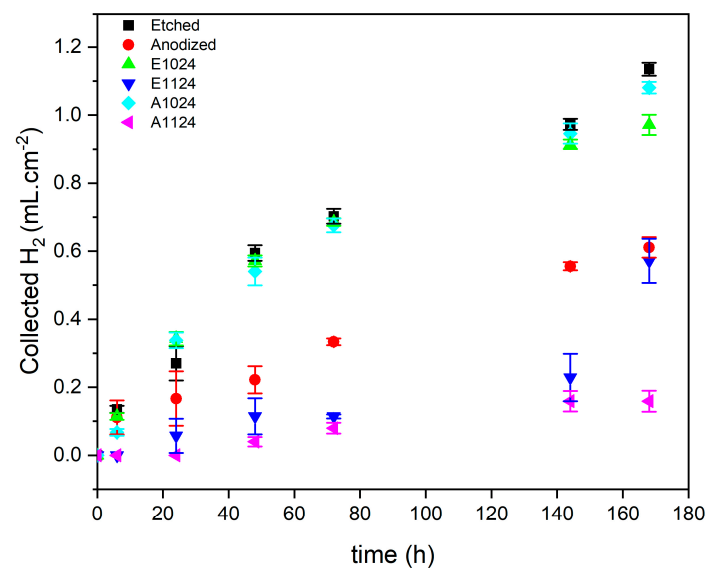
Figure 10. Results of collected H$_2$ after 7 days immersion in 0.1 M NaCl solution.

The experimental data related to the accumulated hydrogen were fitted by a line to have an estimation for corrosion rate. Table 5 shows the mass loss rate, the equations for each estimated line, and R-squared (R^2) as a parameter for showing how close the data are to the modeled line (closer to 1 better the fitting). In these equations, y and t represent the volume of produced hydrogen per surface unit (mL/cm^2) and immersion time (h), respectively. The slope of these lines can be used as an approximation of the corrosion rate of samples due to having the unit of mL·h^{-1}·cm^{-2}. The least collected hydrogen is for LDH samples produced on AZ31 Mg alloy at pH = 11 and previously anodized. The high amount of collected hydrogen for samples E1024 and A1024 shows poor corrosion resistance of these samples while immersed in NaCl solution. As can be observed, the trend of the corrosion rate for samples is as follows: Etched > A1024 > E1024 > Anodized > E1124 > A1124. This result indicates that the compact structure of the LDH outer layer of the samples treated at pH = 11 allows to significantly reduce the corrosion rate and to protect the magnesium substrate by formation of more isolating layer related to the decrease of the lateral size of LDH. Even if the anodizing layer increases the total thickness of the layer, this layer is only slightly more protective and does not play a significant role on the LDH morphology.

Table 5. Weight loss rate and equations of fitted line for hydrogen evolution experimental data.

Sample Code	Weight Loss Rate/ Corrosion Rate (µg·h^{-1}·cm^{-2})	Equation [H (mL/cm^2), t (h)]	R^2
Etched	6.7 ± 0.1	H = 0.0061 t + 0.1564	0.93
Anodized	3.5 ± 0.1	H = 0.0034 t + 0.0624	0.97
E1024	5.7 ± 0.1	H = 0.0054 t + 0.1591	0.9
E1124	3.3 ± 0.2	H = 0.0027 t − 0.0246	0.82
A1024	6.3 ± 0.1	H = 0.006 t + 0.1234	0.94
A1124	0.9 ± 0.08	H = 0.0011 t − 0.008	0.97

3.3. Electrochemical Test of LDH Samples

The Bode and Nyquist diagrams obtained from the EIS test, for etched AZ31 substrate, anodized, and samples with LDH immersed in 0.1 M NaCl solution for 1 h, 6 h, and 24 h are presented in Figures 11 and 12. Generally, the systems with the higher Z modulus at lower frequencies and the higher value of charge transfer resistance exhibit higher corrosion resistance [22,39]. For etched and anodized AZ31 samples, the impedance diagram shows the modulus at low frequency is in the order of 10^3 Ω·cm^2 and the impedance magnitude

was increased after 24 h due to the formation of corrosion products and decrease in active areas [40].

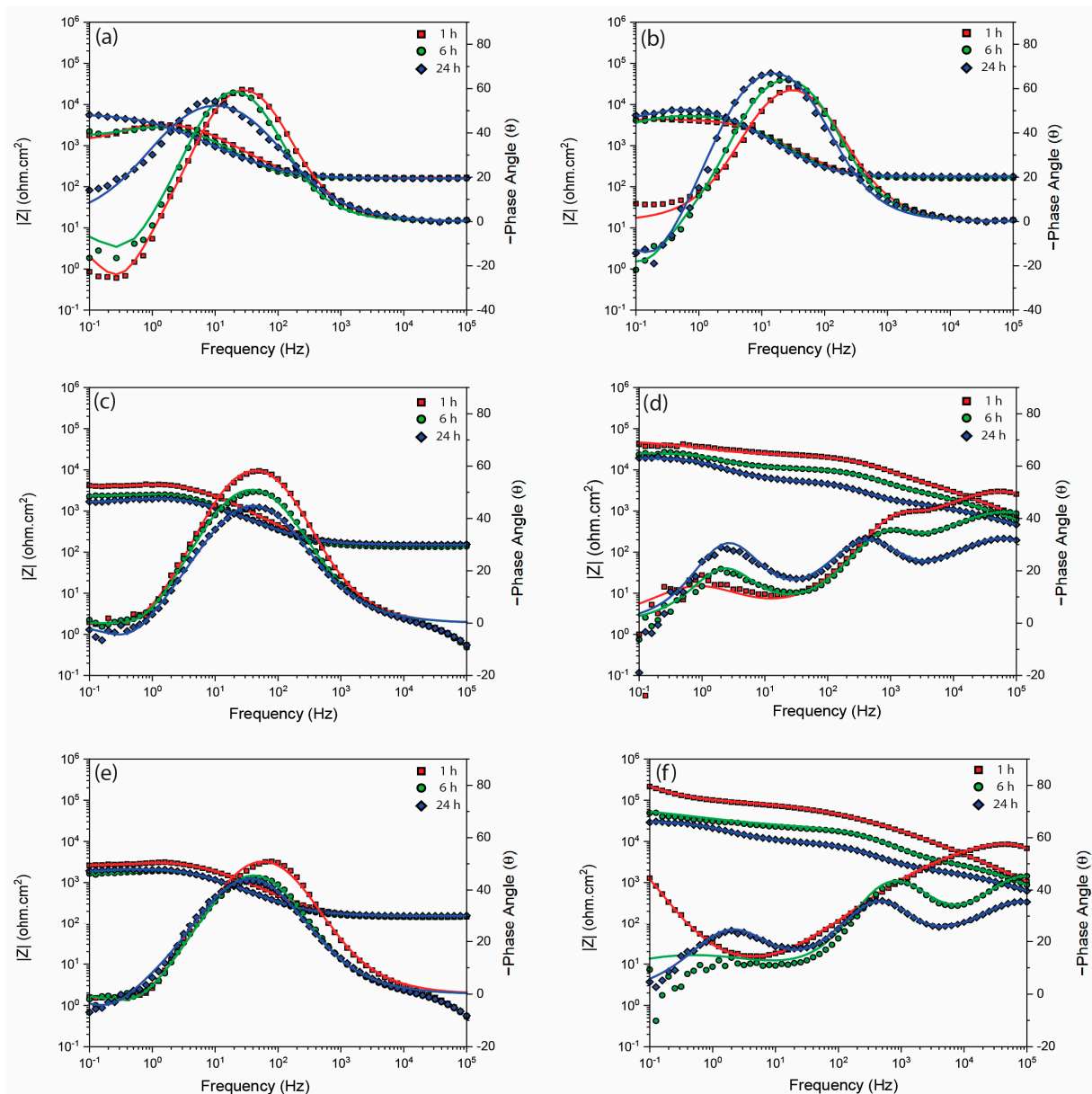**Figure 11.** Bode plots of (**a**) the etched substrate, (**b**) anodized substrate, (**c**) E1024, (**d**) E1124, (**e**) A1024, and (**f**) A1124, after immersion in 0.1 NaCl for 1 h, 6 h, and 24 h.

It can be seen that for LDH samples at pH = 10 on both etched and anodized substrates, the impedance modulus at low frequency remained at the order of 10^3 $\Omega \cdot cm^2$ after 24 h. However, for samples A1124 and E1124, the impedance is around 2.89×10^4 and 1.92×10^4 $\Omega \cdot cm^2$ after 24 h, respectively, which is a bit larger for the anodized samples.

The phase angle at high frequencies can be used to assess the integrity of coatings (LDHs structure) when exposed to corrosive electrolytes [32]. The phase angle at high frequency for AZ31, E1024, and A1024 close to zero demonstrate complete penetration of corrosive ions to the porous layer [41] while for E1124 and A1124 phase angle is less than 0 (around $-50°$ and $-58°$ for E1124 and A1124, respectively), manifesting that the coating has a higher capacitive behavior, unlike E1024 and A1024.
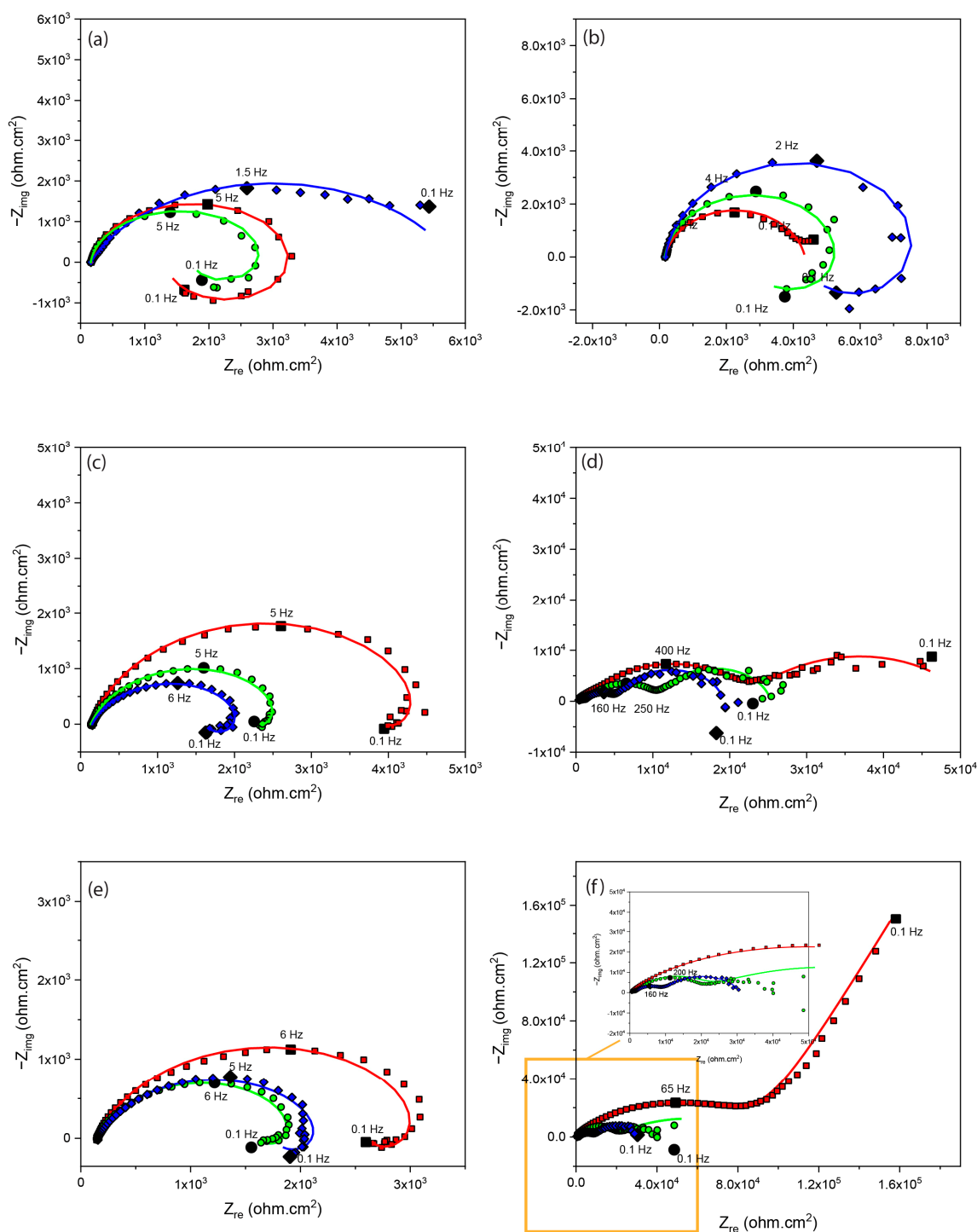
Figure 12. Nyquist plots of (**a**) the etched substrate, (**b**) anodized substrate, (**c**) E1024, (**d**) E1124, (**e**) A1024, and (**f**) A1124, after immersion in 0.1 NaCl for 1 h, 6 h, and 24 h.

The time constant at the low frequency of the Bode and Nyquist phase diagrams shows the inductive loop which is due to the adsorption and coverage of Mg ions, involving monovalent and divalent ions, on the surface of etched, anodized, E1024, and A1024 substrates. For these samples, after 6 and 24 h of immersion, the inductive loop still existed, which points out the poor protective properties of the LDH layer. According to the literature, this loop is attributed to the high concentration of magnesium ions in relatively film-free areas or the relaxation of $Mg(OH)^+$, and Mg^+ absorbed at the surface [42–44]. The other time constant for these samples at medium frequency is a capacitance loop with a

peak at around $-60°$, which can be associated with the response of the charge transfer resistance and the double layer capacitance at the metal/solution interface [27,40].

By increasing the pH of the LDH solution to 11, the inductive loop was less visible until it disappeared for A1124. This shows increased corrosion resistance of substrates by producing LDH at pH = 11 due to the decrease of the lateral size of LDH outer layer and the formation of a more compact layer. Moreover, for samples prepared at pH = 11, we have three time constants (while there are two time constants for samples prepared at pH = 10) which depend on the single or multi-layered structure, and the charge transfer process (the time constants will be discussed in the following paragraphs) [32,45].

The EIS diagrams were fitted by three equivalent circuits Figure 13 and Table 6 present the corresponding fitted data. The EIS test can predict faradaic and non-faradaic components of an electrochemical process [46]. In a faradaic process, the charges can move directly across the metal/solution interface, while in a non-faradaic process, the movement of charges is delayed due to the adsorbed charged molecules at the interface. For this reason, faradic and non-faradaic processes show resistor and capacitor behaviors, respectively. However, experimental results demonstrated that the capacitor, non-ideally, shifts the phase of signals by $n\pi/2$ and called it a constant phase element (CPE). n value varies between 0 and 1 which corresponds to pure resistance and pure capacitance, respectively. The impedance for CPE is shown by the equation below:

$$Z_{CPE} = [Y_0.(i.\omega)^n]^{-1} \tag{5}$$

In this equation Y_0, and n are characteristic parameters of the CPE [47].

In circuit (a), R_s corresponds to the electrolyte resistance, CPE_{dl} is the constant phase element relative to the interface phenomenon (electrochemical double layer), and R_{ct} is the charge transfer resistance. R_1 is a resistance associated with the inductance (L_1) [48]. This model was used for fitting bare samples and the LDH prepared at pH = 10 on etched and anodized samples. However, for etched substrate immersing for 24 h, circuit (b) was used as there was no inductive loop.

The equivalent circuit (c) in Figure 13 is used for E1124 and A1124 samples in which R_{out} and R_{in} are used as parameters to reflect the barrier properties of the outer porous and inner dense layers of the coatings, respectively, and their parallel corresponding CPE for reflecting the heterogeneity of coatings [32,49]. R_{out} and CPE_{out} define the behavior of the layers at high frequency while the time constant at medium frequency is described by R_{in} and CPE_{in} [45]. CPE_{dl} and R_{ct} are the parameters that reveal the electrical double layer capacitance at the interface and the resistance of the electron transfer across the metal surface, respectively. Also, the R_{ct} is inversely proportional to the corrosion rate as it is related to the oxidation of magnesium. The general formula for pure capacitance is as follows:

$$C = \varepsilon \varepsilon_0 A/d \tag{6}$$

In this equation, ε, ε_0, A, and d represent the dielectric constant of medium and vacuum, testing area, and distance, respectively [50]. According to this equation, the capacitance would decrease by increasing distance and decreasing surface. As shown in Table 6, the value of CPE_{dl} for E1124 and A1124 is in order of 10^{-7} $\Omega^{-1} \cdot s^n \cdot cm^{-2}$ which can be attributed to the small-exposed surface caused by the protective layer. For sample E1124 at 1h and 6h, the n value is 1 for CPE_{dl} which is representative of a purely capacitive behavior. For the bare substrate and the samples prepared at pH = 10, the CPE_{dl} is approximately two orders of magnitude higher than E1124 and A1124. This is due to the increased exposed area to the aggressive solution caused by an unprotective layer.
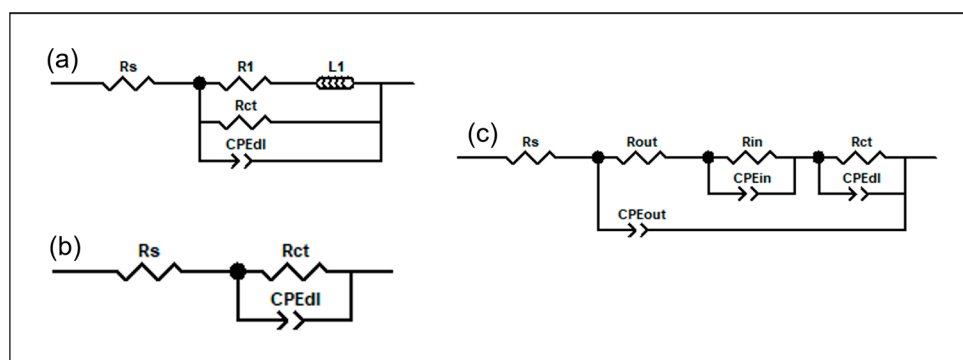
Figure 13. Equivalent circuits used for fitting the electrochemical impedance diagrams.

Table 6. Results of fitted EIS diagrams for the etched and anodized substrates and LDH films at different immersion times.

Sample	R1 ($\Omega\cdot cm^2$)	L1 (Henry)	R_{out} ($\Omega\cdot cm^2$)	CPE_{out} ($\Omega^{-1}\cdot s^n\cdot cm^{-2}$)	n	R_{in} ($\Omega\cdot cm^2$)	CPE_{in} ($\Omega^{-1}\cdot s^n\cdot cm^{-2}$)	n	R_{ct} ($\Omega\cdot cm^2$)	CPE/C ($\Omega^{-1}\cdot s^n\cdot cm^{-2}$)	n
AZ31–1 h	1861	1736	–	–	–	–	–	–	3247	1.12×10^{-5}	0.93
AZ31–6 h	3743	2227	–	–	–	–	–	–	2832	1.64×10^{-5}	0.93
AZ31–24 h	–	–	–	–	–	–	–	–	5670	4.43×10^{-5}	0.71
Anodized−1 h	4.89×10^{-5}	4287	–	–	–	–	–	–	4217	1.10×10^{-5}	0.89
Anodized−6 h	4941	9503	–	–	–	–	–	–	5289	1.03×10^{-5}	0.92
Anodized−24 h	8793	10,254	–	–	–	–	–	–	8052	1.20×10^{-5}	0.92
E1024–1 h	24,700	7285	–	–	–	–	–	–	4848	1.01×10^{-5}	0.85
E1024–6 h	11,969	2888	–	–	–	–	–	–	2724	2.01×10^{-5}	0.80
E1024–24 h	5428	2208	–	–	–	–	–	–	2097	2.50×10^{-5}	0.78
E1124–1 h	–	–	11,705	2.19×10^{-7}	0.64	27,218	1.69×10^{-5}	0.70	12187	1.26×10^{-8}	–
E1124–6 h	–	–	5434	5.75×10^{-7}	0.59	13,412	8.71×10^{-6}	0.94	6442	3.81×10^{-8}	–
E1124–24 h	–	–	1482	2.99×10^{-7}	0.68	13,436	1.00×10^{-5}	0.93	4056	5.83×10^{-8}	0.84
A1024–1 h	11,824	3677	–	–	–	–	–	–	3194	1.38×10^{-5}	0.79
A1024–6 h	6763	2026	–	–	–	–	–	–	1959	2.39×10^{-5}	0.79
A1024–24 h	6990	5741	–	–	–	–	–	–	2140	2.77×10^{-5}	0.77
A1124–1 h	–	–	3381	1.19×10^{-8}	0.84	4.2×10^9	8.7×10^{-6}	0.74	92,037	5.2×10^{-7}	0.48
A1124–6 h	–	–	2933	3.3×10^{-8}	0.78	72,304	2.0×10^{-5}	0.42	15,867	9.4×10^{-8}	0.87
A1124–24	–	–	2219	2.67×10^{-7}	0.65	21,183	2.48×10^{-7}	0.80	7342	3.06×10^{-7}	0.85

Figure 14 shows impedance modulus at the frequency of 0.1 Hz and R_{ct} values for all the samples as well as R_{in} and R_{out} for E1124 and A1124 (Table 6). For etched and anodized AZ31, R_{ct} was increased with immersion time (Figure 14b). This means by increasing immersion time a $Mg(OH)_2$ layer can be produced on the surface of the substrate and slightly protects it from corrosion [51]. For E1024 and A1024, after 24 h immersion, the R_{ct} reduced from 4.84×10^3 and 3.19×10^3 $\Omega\cdot cm^2$ to 2097 and 2140 $\Omega\cdot cm^2$, respectively which is less than the etched and anodized substrates. This indicates the inability of LDH at pH = 10 for protecting substrates which can be attributed to the large lateral size and less dense structure of LDH sheets which leads to partial and incomplete coverage of the surface as well as weak adhesion of the A1024 and E1024 than A1124 and E1124. These layers are not protective and hinder the uniform growth of $Mg(OH)_2$ produced by the corrosion of the substrate and cannot improve the layer barrier properties with immersion time contrary to the cases of etched and anodized samples. As a result, corrosive species can penetrate easily through LDH and reduce the corrosion resistance of substrates. It was visually observed that after the addition of NaCl solution to the electrochemical cell, the solution was spread on the surface of the samples prepared at pH = 10. This can be the result of increased roughness of the surface at this pH due to the fact that increasing roughness will increase hydrophilicity for surfaces with a contact angle of less than 90 degrees [28].

According to Table 6 and Figure 14b, the R_{ct} after 1h immersion for E1124 and A1124 was 1.21×10^4 and 9.20×10^4 $\Omega\cdot cm^2$, respectively, which shows a considerable increase in comparison to E1024 and A1024. This increase shows good corrosion resistance of produced LDH at pH = 11. At this condition, the smaller lateral sheet size led to the denser coating

regarding the SEM micrographs (Figure 2 SEM). After 24 h immersion, R_{ct} for E1124 and A1124 was 4056 and 7342 $\Omega \cdot cm^2$, respectively, which indicates the effectiveness of LDH on the substrates. Moreover, the impedance modulus at low frequency after 24 h for A1124 is only 1.5 times more than E1124 while this value is 15 times more than A1024. This result shows the more significant effect of pH used during the LDH synthesis on the corrosion performance of the layer than the application of a previous anodic treatment at low voltage.
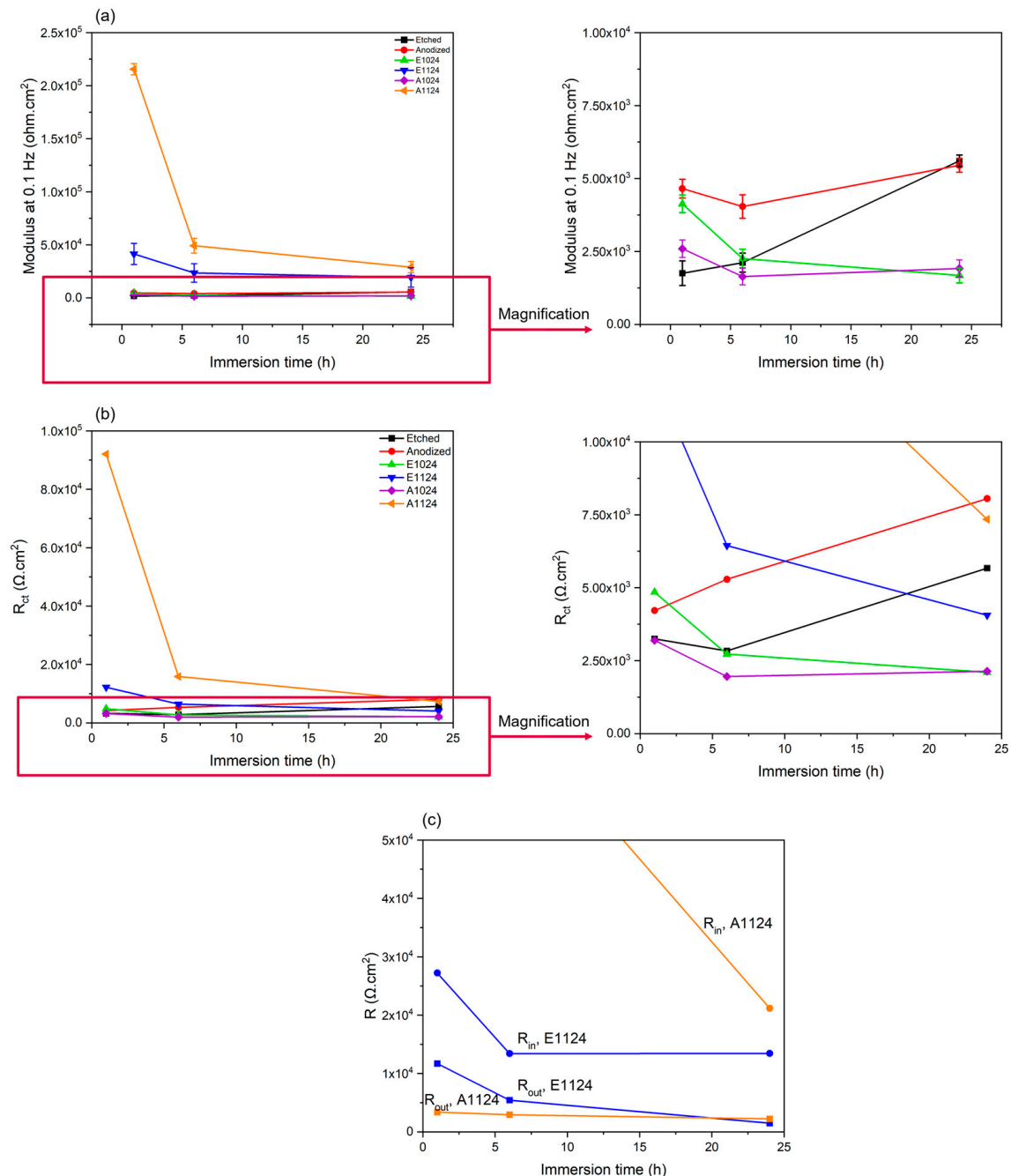

Figure 14. (**a**) Impedance modulus of samples at low frequency (0.1 Hz), (**b**) R_{ct}, (**c**) R_{in} and R_{out}, with different immersion times.

However, in the case of LDH on the surface, the nanostructured film obtained at pH = 11 acts as a barrier for preventing the penetration of corrosive Cl^- ions to the substrate and induces a dense outer layer and a more compact inner layer with measurable values in these conditions (Figure 14c). Moreover, Cl^- ions diffused to the interface of coatings can be trapped into the interlayer and replaced NO_3^-, CO_3^{2-}, or OH^- anions due to the ion

exchangeability of the LDH [41,52,53]. These anions can make a boundary layer by forming $Mg(OH)_2$ or $MgCO_3$ precipitates and repairing existing microcracks in the film [54].

The better corrosion resistance of A1124 can be observed in Figure 14. It can be concluded that in this case, the effect of pH on the size of LDH and corrosion protection is more considerable than surface treatment. In the work of Wu et al. [14] with the Mg-Al/LDH, the EIS results showed a close amount of impedance modulus at low frequency for samples prepared at pH = 10 and 11 with nearly the same LDH lateral size. However, in this study, there is a big difference between the corrosion resistance of LDH prepared at pH = 10 and 11 (obtained from EIS and evolved H_2 results) which can be attributed to the lateral size difference.

3.4. Salt Spray Results

The corrosion behavior of samples with and without epoxy coating was tested using the salt spray test. For this purpose, etched, anodized, and A1124, as the best anti-corrosive LDH sample with the most impedance modulus at the frequency of 0.1 Hz after 24 h (2.9×10^4 $\Omega \cdot cm^2$), were used. The results in Figure 15 show severe corrosion for etched and anodized samples after 6 h of exposure, while for A1124 after 1 day small pits were seen. For the samples with epoxy, etched and anodized substrates failed after 14 days while for the A1124/Epoxy corrosion couldn't be observed even after 35 days.
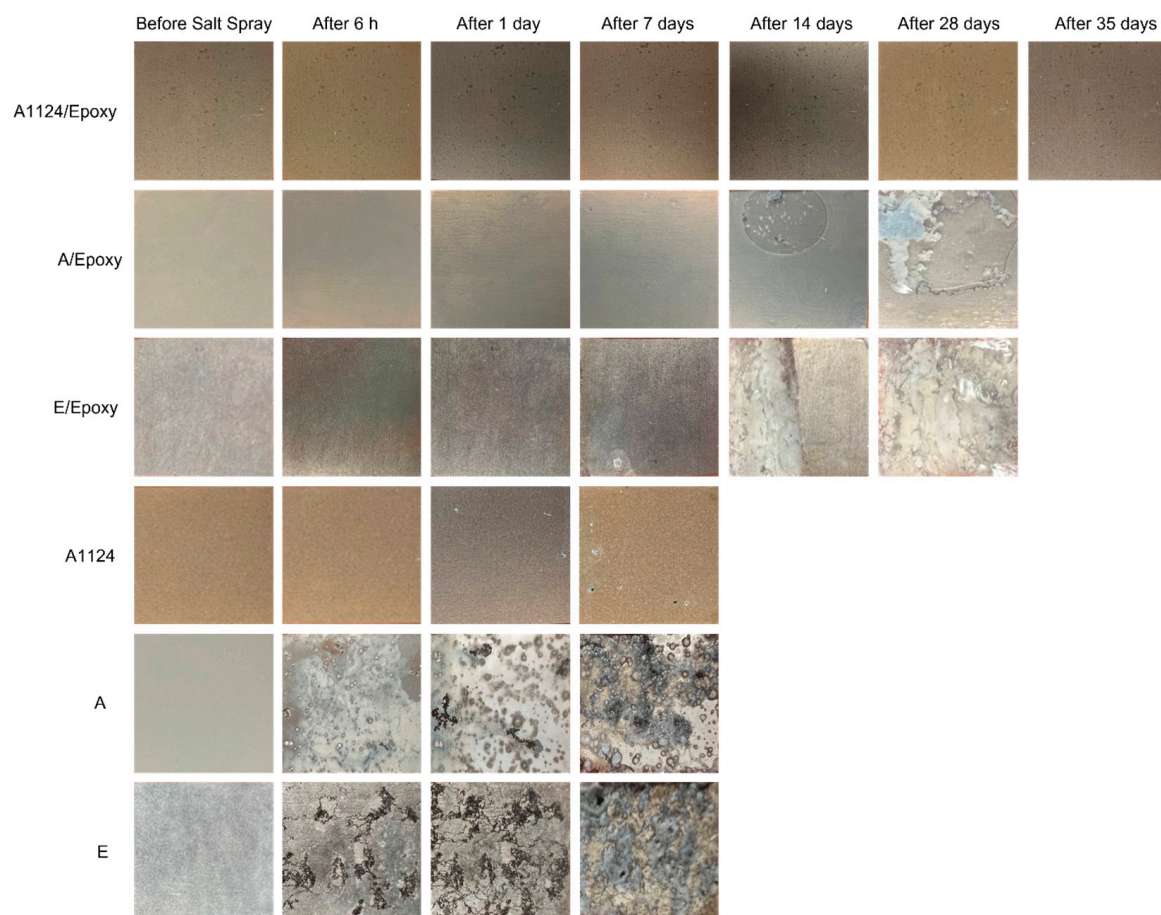

Figure 15. Macroscopic images of the intact samples after salt spray test.

The salt spray test was also performed on x-cut samples with epoxy coating. The better corrosion resistance of A1124/Epoxy was observed according to Figure 16 by having fewer corrosion products on the cuts in comparison to Etched/Epoxy and Anodized/Epoxy. These results show good corrosion protection and compatibility of the LDH layer with the epoxy coating.

Figure 16. Macroscopic images of the x-cut samples after salt spray test.

4. Discussion

For the formation of LDH, first the anodic coating or etched surface of AZ31 would be dissolved in a sufficient alkaline solution and form Mg^{2+} and OH^- [55]. The chemical and physical morphology of LDH is transformed according to the OH^- concentration [55]. At high pH, temperature, and pressure (the condition inside of autoclave) more Mg is dissolved and there are more Mg^{2+} cations [14]. To test this claim, the same procedure as LDH production was repeated on etched and anodized substrates but this time without $Al(NO_3)_3$ compound in the solution. According to Chen et al. [55] when there aren't any extra Al compounds in the solution, $MgAl_2(OH)_8 \cdot H_2O$ as Al-rich compound, and consequently, LDH cannot be formed. Therefore, only a small amount of Mg-rich compound ($Mg_2Al(OH)_7$) can be transferred to $Mg_2CO_3(OH)_2 \cdot 3H_2O$ and $Al_5(OH)_{13}(CO_3) \cdot 5H_2O$ [55], and the top layer is covered by Mg compounds. In Figure 17 cross-section SEM images and EDS of these samples can be seen.

In these images, unlike samples with LDH, the Al elements are evenly distributed and not concentrated on the surface. Moreover, the top layer containing Mg and O elements, shows a larger thickness at pH = 11, illustrating the existence of more Mg at this pH (moreover, $Mg(OH)_2$ is thermodynamically stable at pH > 10.2 [56] and has low solubility in water, with a solubility product constant of 1.5×10^{-11} [57]). For this reason, while the formation of LDH at pH = 11, there would be more Mg^{2+} cations. By having more concentration of Mg^{2+}, the structure is changed to a smaller lateral size to have more area between the substrate and newly formed LDH for consuming Mg cations. Moreover, according to Olf et al. [58], the lower concentration of effective OH^- in weak bases increases the growth and decreases the nucleation of crystals while for the strong base (higher effective OH^- concentration) the nucleation of crystals increases. When the nucleation rate is higher than the growth rate small-sized crystals are made at the same time, however, at a slow nucleation rate, fewer crystals with bigger sizes are formed [59]. Therefore, we can conclude that at pH = 11 nucleation is more than pH = 10 which leads to a smaller size LDH. As a reason, small-sized LDHs would be produced which are more compact and can cover the surface better than bigger-sized LDH and are more protective (as previously proved) against corrosion.
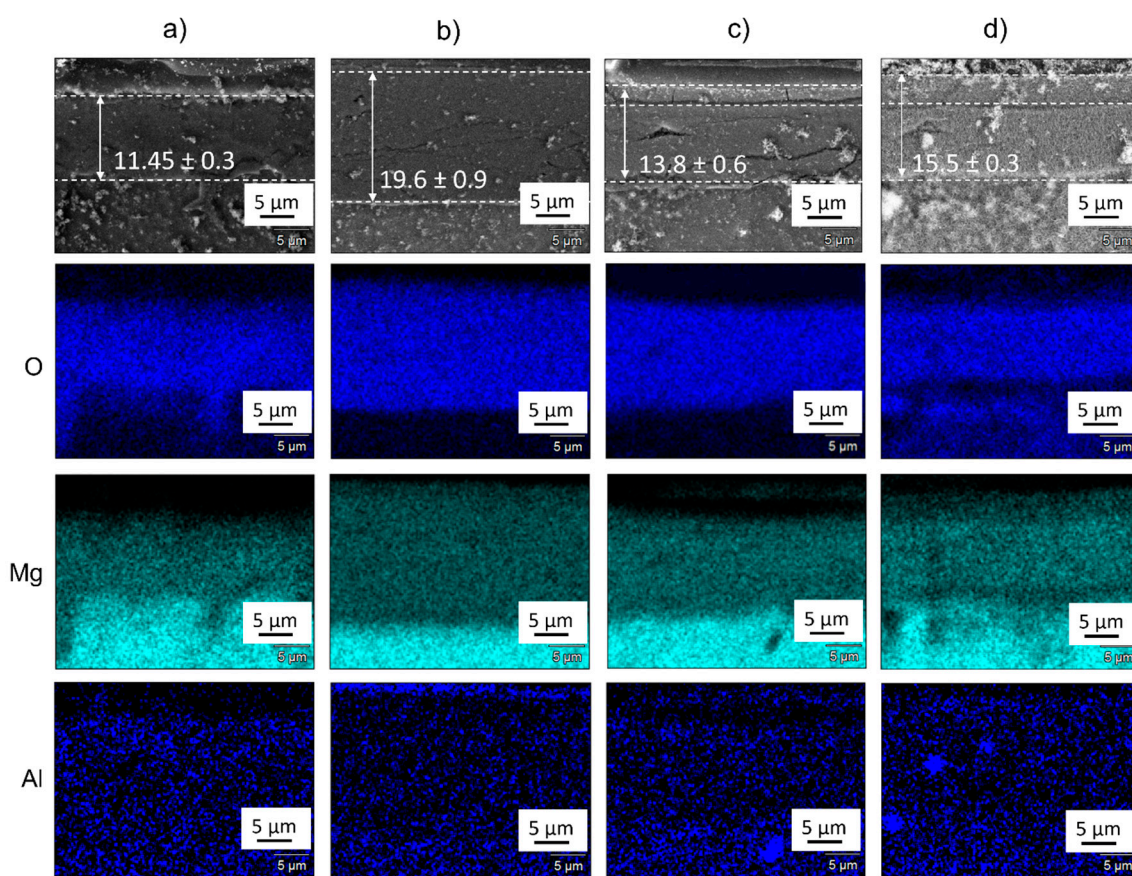
Figure 17. EDS mapping of the cross-section of samples without Al(NO$_3$)$_3$ on (**a**) etched at pH = 10, (**b**) etched at pH = 11, (**c**) anodized at pH = 10, (**d**) anodized at pH = 11.

5. Conclusions

The Mg-Al/LDH films were successfully produced on AZ31 magnesium alloy with different surface treatments by in-situ hydrothermal treatment at pH 10 and 11. Surface morphology, crystalline structure, and corrosion properties were investigated for each sample. The results showed that the lateral and crystal size of LDH and corrosion resistance were affected by pH changes more than surface treatment. LDH prepared at pH = 11 had small size, dense, uniform structure, and good adhesion to the substrate that could protect penetration of corrosive species more than samples prepared at pH = 10. Anodic coating prior to the formation of LDH could slightly enhance the corrosion resistance of substrates. The LDH sample showing the most improved corrosion performance was used for surface pretreatment before applying epoxy resin. The adhesion and compatibility of the epoxy coating applied on prior anodized samples are strongly improved by LDH growth at pH 11.

Author Contributions: R.M.: Investigation, Methodology, Formal analysis, Validation, Writing—Original draft Preparation, Y.P.: Investigation, Validation, L.P.: Methodology, Validation, M.G.: Investigation, Validation, M.-G.O.: Conceptualization, Methodology, Validation, Writing—review and editing, supervision, funding acquisition. All authors have read and agreed to the published version of the manuscript.

Data Availability Statement: The data presented in this study are available on request from the corresponding author.

References

1. Grand View Research. Magnesium Alloys Market Size, Share & Trends Analysis Report by Application (Automotive & Transportation, Aerospace & Defense, Electronics), by Region (MEA, North America, APAC), and Segment Forecasts. 2020–2027. 2016–2018. Available online: https://www.grandviewresearch.com/industry-analysis/magnesium-alloys-market#. (accessed on 14 November 2022).

2. Zaffora, A.; Di Franco, F.; Virtù, D.; Carfì Pavia, F.; Ghersi, G.; Virtanen, S.; Santamaria, M. Tuning of the Mg alloy AZ31 anodizing process for biodegradable implants. *ACS Appl. Mater. Interfaces* **2021**, *13*, 12866–12876. [CrossRef] [PubMed]

3. Joost, W.J.; Krajewski, P.E. Towards magnesium alloys for high-volume automotive applications. *Scr. Mater.* **2017**, *128*, 107–112. [CrossRef]

4. Song, G.L.; Atrens, A. Corrosion mechanisms of magnesium alloys. *Adv. Eng. Mater.* **1999**, *1*, 11–33. [CrossRef]

5. Pardo, A.; Merino, M.; Coy, A.E.; Arrabal, R.; Viejo, F.; Matykina, E. Corrosion behaviour of magnesium/aluminium alloys in 3.5 wt.% NaCl. *Corros. Sci.* **2008**, *50*, 823–834. [CrossRef]

6. Shuai, C.; Yang, Y.; Wu, P.; Lin, X.; Liu, Y.; Zhou, Y.; Feng, P.; Liu, X.; Peng, S. Laser rapid solidification improves corrosion behavior of Mg-Zn-Zr alloy. *J. Alloys Compd.* **2017**, *691*, 961–969. [CrossRef]

7. Song, G.-L. "Electroless" deposition of a pre-film of electrophoresis coating and its corrosion resistance on a Mg alloy. *Electrochim. Acta* **2010**, *55*, 2258–2268. [CrossRef]

8. Toorani, M.; Aliofkhazraei, M.; Mahdavian, M.; Naderi, R. Effective PEO/Silane pretreatment of epoxy coating applied on AZ31B Mg alloy for corrosion protection. *Corros. Sci.* **2020**, *169*, 108608. [CrossRef]

9. Lu, X.; Zuo, Y.; Zhao, X.; Tang, Y. The improved performance of a Mg-rich epoxy coating on AZ91D magnesium alloy by silane pretreatment. *Corros. Sci.* **2012**, *60*, 165–172. [CrossRef]

10. Conceicao, T.F.; Scharnagl, N.; Blawert, C.; Dietzel, W.; Kainer, K.U. Corrosion protection of magnesium alloy AZ31 sheets by spin coating process with poly(ether imide) [PEI]. *Corros. Sci.* **2010**, *52*, 2066–2079. [CrossRef]

11. Pereda, M.D.; Alonso, C.; Gamero, M.; Del Valle, J.; De Mele, M.F.L. Comparative study of fluoride conversion coatings formed on biodegradable powder metallurgy Mg: The effect of chlorides at physiological level. *Mater. Sci. Eng. C* **2011**, *31*, 858–865. [CrossRef]

12. Chen, X.B.; Nisbet, D.R.; Li, R.W.; Smith, P.; Abbott, T.B.; Easton, M.A.; Zhang, D.-H.; Birbilis, N. Controlling initial biodegradation of magnesium by a biocompatible strontium phosphate conversion coating. *Acta Biomater.* **2014**, *10*, 1463–1474. [CrossRef]

13. Wang, H.; Chen, Z.; Cheng, Y. Optimisation of anodising electrolyte for magnesium alloy AZ31 and characteristics of anodic film. *Surf. Eng.* **2010**, *26*, 334–339. [CrossRef]

14. Wu, L.; Pan, F.; Liu, Y.; Zhang, G.; Tang, A.; Atrens, A. Influence of pH on the growth behaviour of Mg–Al LDH films. *Surf. Eng.* **2018**, *34*, 674–681. [CrossRef]

15. Wu, L.; Zheng, Z.; Pan, F.; Tang, A.; Zhang, G.; Liu, L. Influence of reaction temperature on the controlled growth of Mg-Al LDH film. *Int. J. Electrochem. Sci.* **2017**, *12*, 6352–6364. [CrossRef]

16. Zhang, G.; Wu, L.; Tang, A.; Zhang, S.; Yuan, B.; Zheng, Z.; Pan, F. A novel approach to fabricate protective layered double hydroxide films on the surface of anodized Mg-Al alloy. *Adv. Mater. Interfaces* **2017**, *4*, 1700163. [CrossRef]

17. Mishra, G.; Dash, B.; Pandey, S. Layered double hydroxides: A brief review from fundamentals to application as evolving biomaterials. *Appl. Clay Sci.* **2018**, *153*, 172–186. [CrossRef]

18. Kuang, Y.; Zhao, L.; Zhang, S.; Zhang, F.; Dong, M.; Xu, S. Morphologies, preparations and applications of layered double hydroxide micro-/nanostructures. *Materials* **2010**, *3*, 5220–5235. [CrossRef]

19. Kaseem, M.; Ramachandraiah, K.; Hossain, S.; Dikici, B. A Review on LDH-Smart Functionalization of Anodic Films of Mg Alloys. *Nanomaterials* **2021**, *11*, 536. [CrossRef]

20. Shulha, T.N.; Serdechnova, M.; Lamaka, S.V.; Wieland, D.C.F.; Lapko, K.N.; Zheludkevich, M.L. Chelating agent-assisted in situ LDH growth on the surface of magnesium alloy. *Sci. Rep.* **2018**, *8*, 16409. [CrossRef]

21. Wu, L.; Yang, D.; Zhang, G.; Zhang, Z.; Zhang, S.; Tang, A.; Pan, F. Fabrication and characterization of Mg-M layered double hydroxide films on anodized magnesium alloy AZ31. *Appl. Surf. Sci.* **2018**, *431*, 177–186. [CrossRef]

22. Pham, T.T.; Nguyen, T.D.; Nguyen, A.S.; Gonon, M.; To, T.X.H.; Olivier, M.-G. A comparative study of the structure and corrosion resistance of ZnAl hydrotalcite conversion layers at different Al^{3+}/Zn^{2+} ratios on electrogalvanized steel. *Surf. Coat. Technol.* **2022**, *429*, 127948. [CrossRef]

23. Asl, V.Z.; Zhao, J.; Anjum, M.J.; Wei, S.; Wang, W.; Zhao, Z. The effect of cerium cation on the microstructure and anti-corrosion performance of LDH conversion coatings on AZ31 magnesium alloy. *J. Alloys Compd.* **2020**, *821*, 153248. [CrossRef]

24. Yao, Q.-S.; Li, Z.-C.; Qiu, Z.-M.; Zhang, F.; Chen, X.-B.; Chen, D.-C.; Guan, S.-K.; Zeng, R.-C. Corrosion resistance of $Mg(OH)_2$/Mg–Al-layered double hydroxide coatings on magnesium alloy AZ31: Influence of hydrolysis degree of silane. *Rare Met.* **2019**, *38*, 629–641. [CrossRef]

25. Rojas, R. Effect of particle size on copper removal by layered double hydroxides. *Chem. Eng. J.* **2016**, *303*, 331–337. [CrossRef]

26. Guo, Q.; Wang, T.; Zhang, T.C.; Ouyang, L.; Yuan, S. Superhydrophobic double layered MgAl-LDH/epoxy composite coatings for enhanced anticorrosion performance of magnesium alloys. *Prog. Org. Coat.* **2023**, *174*, 107300. [CrossRef]

27. Prince, L.; Rousseau, M.; Noirfalise, X.; Dangreau, L.; Coelho, L.; Olivier, M.-G. Inhibitive effect of sodium carbonate on corrosion of AZ31 magnesium alloy in NaCl solution. *Corros. Sci.* **2021**, *179*, 109131. [CrossRef]

28. Han, X.; Hu, J.; Xiao, T.-B.; Xia, W.; Chen, Y.-N.; Wu, L. Facile fabrication and properties of super-hydrophobic MgAl-LDH films with excellent corrosion resistance on AZ31 magnesium alloy. *Front. Mater.* **2021**, *8*, 545. [CrossRef]

29. Song, G. and Atrens, A. Understanding magnesium corrosion—A framework for improved alloy performance. *Adv. Eng. Mater.* **2003**, *5*, 837–858. [CrossRef]

30. Song, G.; Atrens, A.; StJohn, D. An hydrogen evolution method for the estimation of the corrosion rate of magnesium alloys. In *Essential Readings in Magnesium Technology*; Springer: Berlin/Heidelberg, Germany, 2016; pp. 565–572. [CrossRef]

31. Lin, J.-K.; Jeng, K.-L.; Uan, J.-Y. Crystallization of a chemical conversion layer that forms on AZ91D magnesium alloy in carbonic acid. *Corros. Sci.* **2011**, *53*, 3832–3839. [CrossRef]

32. Dai, X.; Wu, L.; Xia, Y.; Chen, Y.; Zhang, Y.; Jiang, B.; Xie, Z.; Ci, W.; Zhang, G.; Pan, F. Intercalation of Y in Mg-Al layered double hydroxide films on anodized AZ31 and Mg-Y alloys to influence corrosion protective performance. *Appl. Surf. Sci.* **2021**, *551*, 149432. [CrossRef]

33. Pálinkó, I.; Sipos, P.; Berkesi, O.; Varga, G. Distinguishing Anionic Species That Are Intercalated in Layered Double Hydroxides from Those Bound to Their Surface: A Comparative IR Study. *J. Phys. Chem. C* **2022**, *126*, 15254–15262. [CrossRef]

34. Shulha, T.; Serdechnova, M.; Iuzviuk, M.H.; Zobkalo, I.A.; Karlova, P.; Scharnagl, N.; Wieland, D.C.F.; Lamaka, S.V.; Yaremchenko, A.A.; Blawert, C.; et al. In situ formation of LDH-based nanocontainers on the surface of AZ91 magnesium alloy and detailed investigation of their crystal structure. *J. Magnes. Alloys* **2022**, *10*, 1268–1285. [CrossRef]

35. Wang, S.; Liu, C.; Wang, M.; Chuang, Y.; Chiang, P. Arsenate adsorption by Mg/Al–NO$_3$ layered double hydroxides with varying the Mg/Al ratio. *Appl. Clay Sci.* **2009**, *43*, 79–85. [CrossRef]

36. Chen, J.; Fang, L.; Wu, F.; Xie, J.; Hu, J.; Jiang, B.; Luo, H. Corrosion resistance of a self-healing rose-like MgAl-LDH coating intercalated with aspartic acid on AZ31 Mg alloy. *Prog. Org. Coat.* **2019**, *136*, 105234. [CrossRef]

37. Song, Y.; Tang, Y.; Fang, L.; Wu, F.; Zeng, X.; Hu, J.; Zhang, S.F.; Jiang, B.; Luo, H. Enhancement of corrosion resistance of AZ31 Mg alloys by one-step in situ synthesis of ZnAl-LDH films intercalated with organic anions (ASP, La). *J. Magnes. Alloys* **2021**, *9*, 658–667. [CrossRef]

38. Chen, Y.; Wu, L.; Yao, W.; Chen, Y.; Zhong, Z.; Ci, W.; Wu, J.; Xie, Z.; Yuan, Y.; Pan, F. A self-healing corrosion protection coating with graphene oxide carrying 8-hydroxyquinoline doped in layered double hydroxide on a micro-arc oxidation coating. *Corros. Sci.* **2022**, *194*, 109941. [CrossRef]

39. Wu, F.; Liang, J.; Peng, Z.; Liu, B. Electrochemical deposition and characterization of Zn-Al layered double hydroxides (LDHs) films on magnesium alloy. *Appl. Surf. Sci.* **2014**, *313*, 834–840. [CrossRef]

40. Gomes, D.; Borges, C.; Pinto, J.C. Effects of reaction variables on the reproducibility of the syntheses of poly-1,3,4-oxadiazole. *Polymer* **2004**, *45*, 4997–5004. [CrossRef]

41. Chen, J.; Lin, W.; Liang, S.; Zou, L.; Wang, C.; Wang, B.; Yan, M.; Cui, X. Effect of alloy cations on corrosion resistance of LDH/MAO coating on magnesium alloy. *Appl. Surf. Sci.* **2019**, *463*, 535–544. [CrossRef]

42. Song, G.; Atrens, A.; St John, D.; Wu, X.; Nairn, J. The anodic dissolution of magnesium in chloride and sulphate solutions. *Corros. Sci.* **1997**, *39*, 1981–2004. [CrossRef]

43. King, A.D.; Birbilis, N.; Scully, J.R. Accurate Electrochemical Measurement of Magnesium Corrosion Rates; a Combined Impedance, Mass-Loss and Hydrogen Collection Study. *Electrochim. Acta* **2014**, *121*, 394–406. [CrossRef]

44. Prince, L.; Noirfalise, X.; Paint, Y.; Olivier, M. Corrosion mechanisms of AZ31 magnesium alloy: Importance of starting pH and its evolution. *Mater. Corros.* **2022**, *73*, 1615–1630. [CrossRef]

45. Gnedenkov, S.V.; Sinebryukhov, S.L.; Sergienko, V.I. Electrochemical impedance simulation of a metal oxide heterostructure/electrolyte interface: A review. *Russ. J. Electrochem.* **2006**, *42*, 197–211. [CrossRef]

46. Chang, B.-Y. Conversion of a constant phase element to an equivalent capacitor. *J. Electrochem. Sci. Technol.* **2020**, *11*, 318–321. [CrossRef]

47. Zoltowski, P. On the electrical capacitance of interfaces exhibiting constant phase element behaviour. *J. Electroanal. Chem.* **1998**, *443*, 149–154. [CrossRef]

48. Curioni, M.; Salamone, L.; Scenini, F.; Santamaria, M.; Di Natale, M. A mathematical description accounting for the superfluous hydrogen evolution and the inductive behaviour observed during electrochemical measurements on magnesium. *Electrochim. Acta* **2018**, *274*, 343–352. [CrossRef]

49. Asl, V.Z.; Chini, S.F.; Zhao, J.; Palizdar, Y.; Shaker, M.; Sadeghi, A. Corrosion properties and surface free energy of the ZnAl LDH/rGO coating on MAO pretreated AZ31 magnesium alloy. *Surf. Coat. Technol.* **2021**, *426*, 127764. [CrossRef]

50. Deflorian, F.; Fedrizzi, L.; Rossi, S.; Bonora, P. Organic coating capacitance measurement by EIS: Ideal and actual trends. *Electrochim. Acta* **1999**, *44*, 4243–4249. [CrossRef]

51. Galicia, G.; Pébère, N.; Tribollet, B.; Vivier, V. Local and global electrochemical impedances applied to the corrosion behaviour of an AZ91 magnesium alloy. *Corros. Sci.* **2009**, *51*, 1789–1794. [CrossRef]

52. Lin, J.; Hsia, C.; Uan, J. Characterization of Mg,Al-hydrotalcite conversion film on Mg alloy and Cl− and CO32- anion-exchangeability of the film in a corrosive environment. *Scr. Mater.* **2007**, *56*, 927–930. [CrossRef]

53. Zeng, R.-C.; Li, X.-T.; Liu, Z.-G.; Zhang, F.; Li, S.-Q.; Cui, H.-Z. Corrosion resistance of Zn–Al layered double hydroxide/poly (lactic acid) composite coating on magnesium alloy AZ31. *Front. Mater. Sci.* **2015**, *9*, 355–365. [CrossRef]

54. Hu, T.; Ouyang, Y.; Xie, Z.-H.; Wu, L. One-pot scalable in situ growth of highly corrosion-resistant MgAl-LDH/MBT composite coating on magnesium alloy under mild conditions. *J. Mater. Sci. Technol.* **2021**, *92*, 225–235. [CrossRef]

55. Chen, J.; Song, Y.; Shan, D.; Han, E.-H. Study of the in situ growth mechanism of Mg–Al hydrotalcite conversion film on AZ31 magnesium alloy. *Corros. Sci.* **2012**, *63*, 148–158. [CrossRef]

56. Paikaray, S.; Gomez, M.A.; Hendry, M.J.; Essilfie-Dughan, J. Formation mechanism of layered double hydroxides in Mg^{2+}-, Al^{3+}-, and Fe^{3+}-rich aqueous media: Implications for neutralization in acid leach ore milling. *Appl. Clay Sci.* **2014**, *101*, 579–590. [CrossRef]

57. Ropp, R.C. *Encyclopedia of the alkaline earth compounds, Group 16 (O, S, Se, Te) Alkaline Earth Compounds*; Elsevier: Newnes, UK, 2012; p. 118. [CrossRef]

58. Olfs, H.W.; Torres-Dorante, L.O.; Eckelt, R.; Kosslick, H. Comparison of different synthesis routes for Mg–Al layered double hydroxides (LDH): Characterization of the structural phases and anion exchange properties. *Appl. Clay Sci.* **2009**, *43*, 459–464. [CrossRef]

59. Vekilov, P.G. Nucleation. *Cryst. Growth Des.* **2010**, *10*, 5007–5019. [CrossRef]